Modeling the contributions of ring, tail, and magnetopause currents to the corrected *Dst* index

T. Asikainen,[1] V. Maliniemi,[1] and K. Mursula[1]

Received 3 June 2010; revised 3 September 2010; accepted 9 September 2010; published 4 December 2010.

[1] We present a new semiempirical model describing the contributions of the ring, tail, and magnetopause currents to the *Dcx* index. We use the isotropic boundary (IB) location of energetic particles measured by the NOAA/POES satellites, as a proxy for the tail current strength. Using local linear regression, we derive the model parameters and their functional dependencies on solar wind and interplanetary magnetic field parameters and on IB latitude. The model gives the ring, tail, and magnetopause current contributions for the whole time interval 1999–2007, performing roughly equally well during all activity levels. We find that the coefficient of proportionality between the square root of solar wind pressure and the magnetopause current contribution is larger than in earlier estimates. Ring current decay time is found to decrease with increasing solar wind electric field and dynamic pressure. We estimate the average quiet time level of the combined ring and tail (magnetopause) current contributions to *Dcx* to be roughly −7 nT (+13 nT). The average tail current contribution is found to be about 34% of the *Dcx* index, which is somewhat larger than previous estimates based on smaller-intensity storms. For individual storms the tail current contribution can reach up to −160 nT (about 40%–60% of the pressure corrected *Dcx*). The present model agrees well with earlier results for individual storms based on detailed dynamical models of the magnetosphere. Our work demonstrates that the different current contributions to *Dcx* during both active and quiet time intervals can be reliably estimated using solar wind observations and isotropic boundary location.

Citation: Asikainen, T., V. Maliniemi, and K. Mursula (2010), Modeling the contributions of ring, tail, and magnetopause currents to the corrected *Dst* index, *J. Geophys. Res.*, *115*, A12203, doi:10.1029/2010JA015774.

1. Introduction

[2] Geomagnetic storms are the most prominent disturbances of the magnetosphere [*Gonzalez et al.*, 1994]. They are characterized by a fast enhancement of the ring current which is formed of energetic ions and electrons drifting around the Earth typically at radial distances 3–6 R_E (Earth radii). The energetic ions drift westward and the electrons eastward thus creating a westward net current. The enhancement of the ring current results from an increased rate of energy input from the solar wind into the magnetosphere which is mostly thought to be due to enhanced reconnection at the dayside magnetopause during southward interplanetary magnetic field. Typically the dominant source of ring current particles is the nightside plasma sheet from where the particles are injected toward the Earth and consequently energized by substorms and/or enhanced magnetospheric convection. During major magnetic storms the ionospheric oxygen ions can be the dominant ion species in the ring current [*Daglis*, 1997]. After the energy input from the solar wind decreases sufficiently the loss processes of ring current particles start to dominate and the ring current begins to decay. The most important loss processes for ring current particles are collisions with neutral particles of the geocorona (extension of Earth's neutral atmosphere into space), convective losses where the energetic particles drift on open trajectories and escape through the dayside magnetopause and wave-particle interactions which scatter energetic particles into the loss cone.

[3] The *Dst* index [*Sugiura and Kamei*, 1991] was developed to measure the reduction of the horizontal magnetic field component on the ground caused by the westward ring current. The usefulness of the index as an indicator of the ring current is based on the Dessler-Parker-Sckopke relation [*Dessler and Parker*, 1959; *Sckopke*, 1966]

$$\frac{\Delta B_{RC}}{B_0} = -\frac{2W_{RC}}{E_m}, \tag{1}$$

which relates the magnetic field produced by the ring current on the ground ΔB_{RC} to the total kinetic energy content of the ring current W_{RC} (B_0 is the magnetic field intensity at the Earth's equator on the ground level and E_m is the total magnetic energy contained in the magnetic field above the Earth's surface). The minus sign in the equation signifies

[1]Department of Physics, University of Oulu, Oulu, Finland.

that the ring current magnetic field is southward, i.e., opposite to the Earth's internal equatorial magnetic field at the ground level. If the disturbance measured by the *Dst* index is mainly caused by the ring current equation (1) gives a relation between the *Dst* index and the total energy of the ring current.

[4] For decades there has been considerable interest in trying to model and predict the time evolution of the *Dst* index by using measured solar wind and IMF parameters as input. One of the earliest systematic efforts was the study by *Burton et al.* [1975], who used a statistically significant sample of data to construct a semiempirical model describing the evolution of the *Dst* index as a function of solar wind parameters. As was earlier pointed out in several studies [e.g., *Siscoe et al.*, 1968], the currents flowing at the dayside magnetopause produce a northward magnetic field on the ground level and thus give a positive contribution to the *Dst* index that is roughly proportional to the square root of the solar wind dynamic pressure. The effect of the magnetopause currents is most typically seen as an increase in *Dst*, often to highly positive values, when the solar wind dynamic pressure is rapidly enhanced due to a solar wind disturbance (e.g., a coronal mass ejection or a shock wave of a corotating interaction region). Before using *Dst* as a true measure of the ring current one has to correct it for the effect of the solar wind pressure by removing the contribution of the magnetopause currents. Different expressions have been presented in the literature for this correction. In the study by *Burton et al.* [1975] the magnetopause contribution was expressed as $b\sqrt{P_{SW}} - c$, where b = 16 nT/nPa$^{1/2}$ and c = 20 nT. The constant c included the contribution due to the quiet day magnetopause as well as a possible nonzero offset in the *Dst* index itself. A later, more extensive study by *O'Brien and McPherron* [2000] provided quite different values for the two constants, b = 7.26 nT/nPa$^{1/2}$ and c = 11 nT.

[5] *Burton et al.* [1975] assumed that the pressure corrected *Dst* index called *Dst** (that was thought to represent the ring current energy) follows a simple differential equation describing the rate of ring current energy change as the sum of energy input and energy loss

$$\frac{dDst^*}{dt} = F(E_{SW}) - \frac{Dst^*}{\tau}, \tag{2}$$

where $F(E_{SW})$ is a linear function of the solar wind electric field E_{SW} that describes the injection of energy from the solar wind into the ring current and τ is the ring current decay time. They showed that the main features of the time development of the *Dst* index could surprisingly well be reproduced by this simple model. The Burton equation (2) spawned a variety of studies that strived to provide better agreement between the model and the measured *Dst* index. For example, *Gonzalez et al.* [1989] studied a number of storms with different injection functions. They found that especially during intense storms with *Dst* < −100 nT the solar wind pressure enhances the energy injection into the ring current. *O'Brien and McPherron* [2000] used a larger data set to analyze how the solar wind parameters affect the ring current injection and decay. They found that the injection could be represented by a linear function of the solar wind electric field and that the ring current decay time was also dependent on the solar wind electric field, being generally smaller for higher values of the electric field. This explained in their model the typically observed short decay time (2–4 h) at the beginning of the storm recovery phase, when the solar wind electric field starts diminish, and the subsequent slower recovery with a significantly longer decay time (10–20 h). Also other studies have confirmed that the ring current decay time is not constant but depends on the storm (or storm driver) intensity [see, e.g., *Gonzalez et al.*, 1989; *Akasofu*, 1981; *Feldstein et al.*, 1990; *MacMahon and Llop-Romero*, 2008]. Also the increase of the fraction of oxygen ions, with a relatively short life time, in the ring current during large storms can decrease the effective ring current decay time [*Daglis et al.*, 1999]. The *Dst* index was recently also modeled by *Wang et al.* [2003], *Ballatore and Gonzalez* [2003], *Temerin and Li* [2002], and *O'Brien and McPherron* [2002]. *Søraas et al.* [2002] showed that the *Dst* index could also be modeled quite well by using the energetic particle flux measured by the low-altitude NOAA/POES satellites as a measure of energy injection into the ring current.

[6] Being computed from ground level magnetic data the *Dst* index is bound to contain contributions also from other large-scale magnetospheric and ionospheric current systems to some degree. The effect of the largest magnetospheric current system, the magnetotail current (including the tail lobe magnetopause currents) on the *Dst* index was omitted for a long time in all *Dst* models. However, after the development of advanced magnetospheric modeling techniques it was possible to study the tail current effects. An analytical model taking into account the effects of the ring current, the magnetopause currents, the tail current system and the field aligned currents was presented by *Alexeev et al.* [1996, 2001, 2003]. This so-called paraboloid model (A2000) was semiempirical in the sense that it was built upon analytic expressions depending on several parameters that were determined from solar wind and magnetospheric measurements. Using the paraboloid model, *Kalegaev and Makarenkov* [2006] showed that the tail current system can have a highly significant contribution to the *Dst* index during storms of different intensity. They found that during small storms the tail current contribution can dominate the *Dst* index while during intense storms the ring current has the largest effect on *Dst*. Using magnetic field modeling based on Tsyganenko T89 and T96 magnetic field models, *Turner et al.* [2000] showed that the tail current contribution to the *Dst* index is on an average about 25%. It is worthwhile to note that, since their results are based on the T89/T96 magnetic field models the results only apply to the small and moderate magnetic storms with peak *Dst* > −100 nT where the models are valid. Similar modeling work aiming to separate the contributions of the different current systems to *Dst* was done by *Ganushkina et al.* [2004], *Kalegaev et al.* [2005], and *Tsyganenko and Sitnov* [2005], who supported the view that the tail current contribution during moderate storms can be dominant but during intense storms the ring current dominates the *Dst* index.

[7] As discussed above, the *Dst* index is a widely used indicator of the ring current intensity (after the contributions from other current systems have been removed) and is thus an important tool in monitoring the development of magnetic storms. However, the official *Dst* index has been shown to contain both random and systematic errors [*Karinen*

et al., 2002; *Karinen and Mursula*, 2005; *Mursula and Karinen*, 2005; *Mursula et al.*, 2008, 2010]. Among the systematic errors are the erroneous treatment of the Sq variation due to ionospheric currents, the incorrect latitude normalization and the unequal weighting of the individual stations in the index. A more correct version of the *Dst* index called the *Dcx* index has been developed.

[8] In this work we present a new semiempirical model based on a modified Burton equation that separates the contributions of the ring, tail and magnetopause currents to the *Dcx* index. In section 2 we describe how the tail current can be monitored indirectly by low-altitude satellite observations of energetic particles. In section 3 we present the theoretical basis of our model and the data used. In section 4 we discuss the statistical analysis methods used in this work and in section 5 the application of these methods in the determination of the model parameters. In section 6 we reconstruct the *Dcx* index using the model. Section 7 presents our model results for a few individual events. The summary and conclusions are given in section 8.

2. Tail Current Index

[9] The pitch angle distribution of energetic particles measured by low-altitude satellites can provide information about the magnetospheric magnetic field configuration. In the inner magnetosphere where the field lines are roughly dipolar the pitch angle distribution of energetic particles is typically anisotropic with more particles observed at 90° pitch angle than at 0° and 180° directions. However, at the magnetotail where the field lines are highly stretched due to the strong cross-tail current sheet the energetic particle distributions at any point on the closed field lines are typically isotropic. This is due to strong pitch angle scattering in the highly curved magnetic field at the tail current sheet [*Chen*, 1992]. It has numerically been shown that when the radius of curvature of magnetic field lines becomes less than about 8 times the particle gyroradius the particles are effectively scattered [e.g., *Sergeev and Tsyganenko*, 1982]. Accordingly, on the tail side field lines with low invariant latitude the pitch angle distribution is typically anisotropic and becomes isotropic poleward of a rather sharp boundary which is called the isotropic boundary (IB).

[10] The IB can be monitored conveniently by using the low-altitude polar orbiting NOAA/POES satellites. These satellites are Sun synchronous with an altitude of about 850 km. They contain instruments for measuring auroral particles as well as energetic particles from 30 keV upward. The MEPED instrument that measures the energetic particles contains two orthogonally directed detectors that measure the particle flux in local vertical direction (0° detector) that points radially away from Earth and local horizontal direction (90° detector) that points antiparallel to spacecraft velocity. This means that close to the equator the 0° detector measures locally trapped particles and at high latitudes locally precipitating particles. The 90° correspondingly measures locally roughly parallel or antiparallel particles (depending on the direction of spacecraft motion) close to the equator and locally trapped particles at the high latitudes. A comprehensive description of the NOAA/MEPED instrument is given by *Hill et al.* [1985], *Seale and Bushnell* [1987], *Raben et al.* [1995], and *Evans and Greer* [2000]. Although the pitch angles of the detectors change along the orbit the IB can easily be detected by comparing the fluxes of the two orthogonal detectors. *Sergeev and Gvozdevsky* [1995] studied the isotropic boundary using the NOAA/MEPED measurements and they identified the boundary essentially by measuring the corrected geomagnetic latitude (CGMLat) where the ratio of the count rates of the two orthogonal detectors I_0/I_{90} measuring 80 keV protons exceed a certain threshold value (0.7 in their work) as the satellite moves poleward. In this work we have determined the corrected geomagnetic latitude of the IB from the measurements of 80–240 keV protons (2nd energy channel of MEPED) using the following criteria: (1) the count rates at 0° and 90° detectors (I_0 and I_{90}, respectively) fulfill the condition

$$\left|\frac{I_0 - I_{90}}{I_0 + I_{90}}\right| < 0.15 \tag{3}$$

for a duration of 8 s (4 data points) after the first occurrence of a point where the above condition holds, and (2) $I_0 > 5$ cts/s.

[11] After numerous experiments we found these criteria to be more suitable and robust for determining the IB location automatically for a large amount of data than the original algorithm [*Sergeev and Gvozdevsky*, 1995]. It is important to note that the proton detectors in the MEPED instrument onboard NOAA/POES satellites degrade in time due to radiation damage and this degradation leads to erroneously low fluxes already 2–3 years after the satellite launch. We [*Asikainen and Mursula*, 2010] have recently made an extensive study of the effect of radiation on these detectors and introduced a set of calibration factors that can be used to correct the measurements of all the NOAA/POES satellites. We also applied the correction to the full data set of 30 years of NOAA/MEPED data. In this work we use the corrected MEPED proton data. The correction is relevant for the determination of the IB location since the 0° and 90° detectors do not degrade at the same rate (typically the 90° detector degrades faster). This difference distorts the flux ratio determining the IB. Without the correction, the IB location would shift poleward in time and, after sufficient degradation, the IB would not be observed any longer. Furthermore, when using the MEPED proton data it is important to note that the counts measured by the 0° detector are accumulated 1 s earlier than the corresponding count rates at the 90° channel even though they are given the same 90° channel time stamp in the data files [*Evans and Greer*, 2000]. Accordingly, when comparing the two detectors one must shift the 0° measurements backward in time by 1 s.

[12] The usefulness of the IB location as an indicator of the tail current was demonstrated by *Sergeev et al.* [1993], who showed that the IB latitude measured by the MEPED instruments correlates very well with the magnetic field direction measured by GOES near the tail current sheet. The magnetic inclination angle in the tail near the current sheet decreases as the measured IB latitude decreases; that is, when the magnetic field becomes more stretched, the IB shifts to lower latitudes. Since by Ampére's law the tangent of the magnetic inclination angle is inversely proportional to the linear current density in the GSM-Y direction the inverse of the IB latitude reflects the intensity of the current at the near-Earth tail. However, as *Sergeev et al.* [1993] and *Sergeev and Gvozdevsky* [1995] showed, the IB latitude

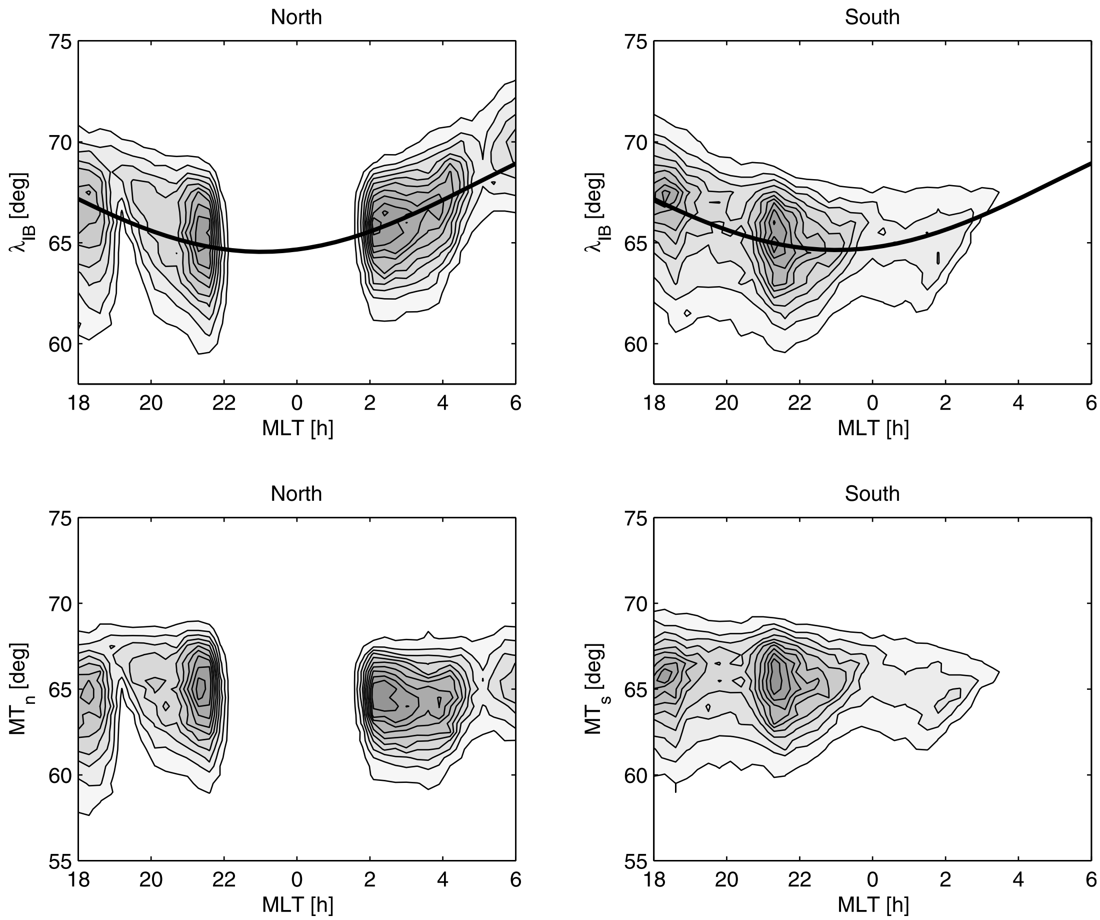

Figure 1. (top) The determined IB latitudes as a function of MLT for the northern and southern hemispheres. (bottom) The MT indices as a function of MLT for the northern and southern hemispheres. Gray-scale shading shows the density of the data points in logarithmic scale.

systematically depends on magnetic local time (MLT), being generally at lower latitudes at midnight and shifting to higher latitudes toward the evening and morning sectors. *Sergeev and Gvozdevsky* [1995] used 1 month of data from the NOAA-6 satellite to determine the MLT dependence of the IB latitude. They constructed a measure of the tail current, the so-called MT-index, by removing the MLT dependence from the measured IB latitudes.

[13] Here we have used the corrected data from NOAA 15, 16, 17, and 18 satellites during 1.1.1999–31.12.2007 to determine the MT-index. Since our data and the time period of interest as well as the criteria for determining the IB latitude are different from those used by *Sergeev and Gvozdevsky* [1995], we determined the MLT dependence of the IB latitude appropriate for our data rather than using their expression. We separately determined the IB location for the northern and the southern hemispheres and found that the MLT variation of the boundary is best removed by the following expressions:

$$MT_n = \lambda_{IB,n} - 3.49\left[1 - \cos\left[\frac{\pi}{12}(MLT - 23.0)\right]\right] \quad (4)$$

$$MT_s = \lambda_{IB,s} - 3.40\left[1 - \cos\left[\frac{\pi}{12}(MLT - 23.0)\right]\right] - 0.09^\circ, \quad (5)$$

where the MT_n and MT_s are the MT indices for the northern and southern hemispheres, respectively, and $\lambda_{IB,n}$ and $\lambda_{IB,s}$ denote the measured IB CGMLat latitudes for the two hemispheres. In finding the MLT variation we only considered the nightside observations (MLT $\geq$ 18 h and MLT $\leq$ 6 h) in order to avoid any bias to the fit from the dayside values that are not directly related to the field line curvature at the nightside. The offset value of $-0.09°$ in the expression for MT_s depicts an average systematic difference of $-0.09°$ between the MT_n and MT_s values. We then calculated the average hourly MT values by taking the average of all MT_n and MT_s values between 18 and 06 MLT measured within each UT hour. The top panels of Figure 1 show the determined IB latitudes for northern and southern hemispheres. (Note that the gaps in the north between 20 and 2 h MLT and in the south between 4 and 6 h MLT are caused by the orbits of NOAA 15–18 s/c that only sample some regions of the MLT latitude plane). The gray-scale shading shows the logarithm of the density of the data points in Figure 1. One can clearly see the systematic dependence of the IB latitude on MLT so that the boundary is at lower latitudes at the nightside than at dawn and dusk. The bottom row panels show similar plots for the MT indices for the northern and southern hemispheres. One can see that the systematic

MLT dependence is effectively removed by equations (4) and (5).

3. Model and Data

[14] Here we develop the work of *Burton et al.* [1975] and *O'Brien and McPherron* [2000] and construct a semiempirical model for the *Dcx* index. We start by expressing the *Dcx* index as a sum:

$$D_{CX} = D_{RC} + D_T + D_{MP} + c, \tag{6}$$

where D_{RC}, D_T and D_{MP} are the contributions of the ring current, the tail current and the magnetopause currents to the *Dcx*. The possible offset in the *Dcx* index due to the quiet time levels of the ring, tail and magnetopause current systems is denoted by the constant c. Note that generally $D_{RC} \leq 0$, $D_{MP} \geq 0$ and $D_T \leq 0$. We describe the time development of the ring current with a Burton-type equation:

$$\frac{dD_{RC}}{dt} = Q - \frac{D_{RC}}{\tau}, \tag{7}$$

where the term Q describes injection of energy into the ring current in units of nT/h and τ is the ring current decay time. On the basis of previous studies [e.g, *Gonzalez et al.*, 1989; *O'Brien and McPherron*, 2000] we assume that the injection function Q and the decay time τ are unknown functions of solar wind electric field E_{SW} and, possibly, of the dynamic pressure P_{SW}. For the tail current contribution we assume for simplicity that D_T is only a function of the MT-index. For the magnetopause currents we make the common assumption that D_{MP} depends only on the square root of solar wind dynamic pressure $\sqrt{P_{SW}}$.

[15] Inserting the expression (6) into equation (7) we obtain the equation for the time development of the *Dcx* index:

$$\frac{dD_{CX}}{dt} = Q + \frac{c}{\tau} - \frac{D_{CX}}{\tau} + \frac{D_{MP}}{\tau} + \frac{D_T}{\tau} + \frac{dD_T}{dMT}\frac{dMT}{dt} + \frac{dD_{MP}}{d\sqrt{P_{SW}}}\frac{d\sqrt{P_{SW}}}{dt}, \tag{8}$$

where the last two terms are the time derivatives of $D_T(MT)$ and $D_{MP}(\sqrt{P_{SW}})$.

[16] The unknown functions $Q(E_{SW}, P_{SW})$, $\tau(E_{SW}, P_{SW})$, $D_T(MT)$, $D_{MP}(\sqrt{P_{SW}})$ and the constant c can be determined using advanced inversion methods and measured data. The time interval studied here (1.1.1999–31.12.2007) contains the most active time of the solar cycle 23 as well as most of its descending phase, being ideally suited to study the solar wind magnetosphere connection during very different levels of geomagnetic activity and solar wind conditions. The hourly solar wind and IMF data were obtained from the OMNI2 database (http://omniweb.gsfc.nasa.gov). We also used the MT index constructed from the NOAA 15, NOAA 16, NOAA 17, and NOAA 18 data as described above, and the most recent version of the hourly *Dcx* index.

[17] Equation (8) contains time derivatives of the measured parameters. In most previous studies [*Burton et al.*, 1975; *O'Brien and McPherron*, 2000] the time derivative of a quantity y at time i has been estimated from the difference $\delta y_i = y_{i+1} - y_i$. However, since y_i indicates the mean value during hour i, the time derivative estimated in this way actually describes the average time rate of change from the middle of hour i to the middle of the next hour $i + 1$, i.e., symmetrically around the end of hour i. This introduces a time offset of 0.5 h between the hourly averages and the corresponding time derivatives. A more appropriate way to calculate the derivative is to use the two point formula for the numerical derivative

$$\frac{\Delta y_i}{\Delta t} = \frac{y_{i+1} - y_{i-1}}{2}, \tag{9}$$

which computes the time rate of change symmetrically around the hour i (time unit is 1 h). Here we have used this method to compute the derivatives in equation (8).

4. Local Linear Regression

[18] In the analysis of equation (8) we have applied the local linear regression which is a nonparametric estimation method. Let us first consider a simple linear model

$$y = ax + b + \varepsilon, \tag{10}$$

where x is the explaining variable, y the response variable, a and b the model parameters and ε a random error term. If a and b can be assumed to be constant they can be easily solved by standard regression of the measured x and y values. However, if a and b are not constant but some unknown functions of a third variable z, the functions $a(z)$ and $b(z)$ cannot be determined by ordinary regression methods. In local linear regression we approximate the unknown parameter functions around a given point $z = z_0$ by a Taylor series:

$$a(z) \approx a(z_0) + a'(z_0)(z - z_0), \tag{11}$$

where $a'(z_0)$ is the derivative of the unknown function $a(z)$ at point $z = z_0$. Writing all the unknown parameter functions as a Taylor series the regression equation becomes

$$y = a(z_0)x + a'(z_0)(z - z_0)x + b(z_0) + b'(z_0)(z - z_0) + \varepsilon, \tag{12}$$

which holds approximately when the values of z are close to z_0. In this regression model we now have three explaining variables x, $(z - z_0)x$ and $(z - z_0)$ and corresponding constant regression coefficients $a(z_0)$, $a'(z_0)$ and $b'(z_0)$ in addition to the constant term $b(z_0)$. These unknown constants can be estimated by selecting from the data only those points where the regression model holds, i.e., points where the values of z are close to z_0, and then performing the usual multivariate linear regression. In practice we first select a value of z_0 and perform the regression using only those points where $|z - z_0| \leq W/2$, where W is the length of the window around z_0. Selecting a number of different values for z_0 and performing the regression for each value we can obtain the parameters a and b (as well as their derivatives) as a function of z_0, i.e., of z. It can easily be shown that the smoothness of estimated parameter functions increases as one increases the window length W. On the other hand increasing the window length too much will compromise the accuracy of the linear Taylor series approximation of the parameter functions. In principle we could include higher-order terms of the Taylor series expression to increase the accuracy for larger window lengths, which would lead to the local polynomial regression method. However, in this work we use the linear approximation.

[19] Using local linear regression with a relatively large window length W it is customary to weight the data points included in the regression by an amount that depends on how much z deviates from z_0. Points that are far away from z_0 will be given a smaller weight in the regression than those points which are close to z_0. One of the weighting functions commonly used in local linear regression is the tricube window which is defined as

$$w(z) = \left(1 - \left|\left(2\frac{z - z_0}{W}\right)^3\right|\right)^3, \text{ for } 2\frac{|z - z_0|}{W} \leq 1 \tag{13}$$

$$w(z) = 0, \text{ for } 2\frac{|z - z_0|}{W} > 1. \tag{14}$$

Such a window has a broad plateau around z_0 where $w \approx 1$ and it smoothly but quite steeply drops to zero. In this work we use the tricube window when performing the local linear regression.

[20] When estimating the parameter (function) values in the regression equation we use the M estimation method that can robustly cope with possible outliers when performing linear regression [*Huber*, 1964]. The idea of the method is to perform a weighted least squares fit with weights that depend on the residuals themselves; that is, points with larger residuals are given a smaller weight. One of the most common weighting functions that we have also used in this work is the bisquare weight function

$$w(e) = \left[1 - \left(\frac{e}{k}\right)^2\right]^2, \text{ for } |e| \leq k \tag{15}$$

$$w(e) = 0, \text{ for } |e| > k, \tag{16}$$

where e is the residual and k is a tuning constant,

$$k = \frac{4.685 \times \mathrm{MAR}}{0.6745}, \tag{17}$$

and MAR denotes the median of absolute residuals. We first perform a normal linear regression and compute the weights based on the obtained residuals. Then we perform the robust regression with the bisquare weights. We continue iteratively by using the residuals of the previous step to calculate the weights for the next step until the regression coefficients converge. When using the robust regression method in combination with the local linear regression we multiply the weights of the local linear regression with those of the robust regression.

5. Determining the Model Parameters

[21] Before discussing the determination of the model parameters, we first note that in the analysis below we found that the determined MT values exhibit large variability from one hourly value to the next (evidently depicting rapid variations in the tail current) without corresponding variations in the *Dcx* index. Since the hourly MT values are typically calculated only from a few individual measurements within each hour the MT-index has a relatively much larger variance than the corresponding solar wind parameters and the *Dcx* index which are averages computed from 1 min data. To reduce the variance of MT from one value to the next we applied a 3 point running mean to the MT time series. The filtered MT describes better the average tail configuration and reduces the effects of rapid tail current dynamics below hourly scale.

[22] Since most of the data are measured during quiet times when the variation in the *Dcx* is not related to storms we decided to use only those data points in our analysis where the $Dcx \leq -30$ nT (roughly 12% of all the data). However, even after discarding almost 88% of the original data we found in the end that the model determined only by this limited, storm time data set produced only a slightly better overall correlation coefficient and a smaller RMS deviation between the modeled and measured *Dcx* indices than the model including also the quiet time data.

[23] Let us now first determine the contribution of the tail current D_T to the *Dcx* by performing a local linear regression to equation (8) assuming that the regression coefficients are functions of the MT index. Our explaining variables are D_{CX}, dMT/dt and $d\sqrt{P_{SW}}/dt$ and the constant term in the equation is $Q + (D_{MP} + D_T + c)/\tau$. We perform the local linear regression by selecting 120 equally spaced values of MT from the range $MT = [47, 75]$ so that the centers of the regression windows are at $MT_i = 47 + 0.2333i$. The length of the window was chosen to be $W = 3$. We note that all those data points were excluded from the regression where any of the values of MT, P_{SW} or their derivatives are missing. Estimating now the regression coefficients for each window yields, among other things, the values of dD_T/dMT as a function of MT. The other regression parameters are also obtained as functions of MT but at this point they only act as dummy variables.

[24] The left-hand side of Figure 2 shows the derivative dD_T/dMT obtained from the local linear regression as a function of MT. The MT values have been calculated as the average of the MT values within each window. Thus the MT values do not necessarily correspond to the central values of the regression windows. We have left out from the plot those derivative values where the number of regression points was below 10 or the relative standard deviation was above 1 (there were 43 such points out of 120). Above MT = 55° the errors of the estimated derivatives are very small while below MT = 55° they are larger. Despite the larger error the larger values of the derivative for small MT values are evident. The right-hand side of Figure 2 shows the integral of the estimated derivative, i.e., the function $D_T(MT)$. The integral

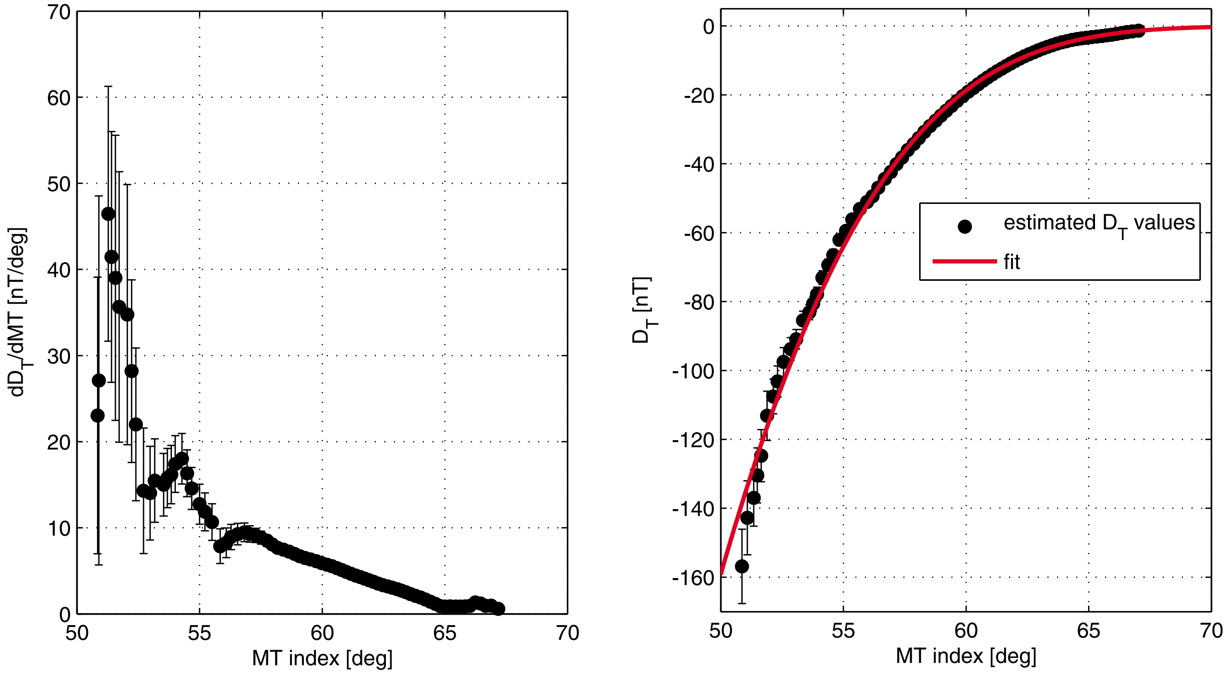

Figure 2. (left) Estimated derivative of $D_T(MT)$ as a function of MT index. (right) Estimated $D_T(MT)$ function (integral of the derivative on the left-hand side).

was calculated numerically from the estimated derivative using the trapezoidal rule. The constant of integration was chosen so that the $D_T = 0$ nT when MT = 75.5 (the maximum value of the MT index in the data corresponding to the quietest state of the tail current). The error of the *j*:th D_T value was estimated by the following expression:

$$\Delta D_{T,j} = \left[\sum_{i=j}^{N} \left(\frac{1}{2} (MT_{i+1} - MT_i)(e_{i+1} + e_i) \right)^2 \right]^{1/2}, \tag{18}$$

where e_i is the error of the *i*:th derivative estimate in the left-hand plot of Figure 2 and $N = 77$ is the number of derivative estimates. The following expression provides a good fit to the estimated D_T:

$$D_T = -5.495 \cdot 10^7 \left[\frac{1}{\cos^2 MT} + 2.633 \right]^{-7.871}, \text{ when } MT \leq 75.5^\circ$$
$$D_T = 0, \text{ otherwise.} \tag{19}$$

The numerical coefficients were determined by minimizing the sum of the squared deviations between the model and the data points. (Note that the $\cos^{-2}(MT)$ term is the L value of a dipolar field line whose invariant latitude is MT). This fit is included in the right side of Figure 2. The most striking feature of the function D_T is its large range extending from 0 nT to about −160 nT. Note also the small error estimates that are less than ±11 nT.

[25] Next we will estimate the contribution of the magnetopause currents to the *Dcx*. Now that D_T has been estimated we can compute its values from the hourly MT values. This allows us to rewrite equation (8) in the form

$$\frac{d(D_{CX} - D_T)}{dt} = Q + \frac{c}{\tau} + \frac{D_{MP}}{\tau} - \frac{(D_{CX} - D_T)}{\tau} + \frac{dD_{MP}}{d\sqrt{P_{SW}}} \frac{d\sqrt{P_{SW}}}{dt}. \tag{20}$$

We now perform the local linear regression to equation (20). Our response variable is now the left-hand side of equation (20), explaining variables are $D_{CX} - D_T$, and $d\sqrt{P_{SW}}/dt$ and the constant term is $Q + (D_{MP} + c)/\tau$. In this regression we exceptionally used only the quiet time data where $Dcx > -30$ nT because the effect of magnetopause currents on the *Dcx* is more evident during such times than during storms. We now select 80 equally spaced values of $\sqrt{P_{SW}}$ from the range $\sqrt{P_{SW}} = [0, 8]$ in units of $\mathrm{nPa}^{1/2}$ (almost all data points fall within this range), so that the centers of the regression windows are given by $\sqrt{P_{SW_i}} = 0.1i$. The length of the window was chosen to be 2 $\mathrm{nPa}^{1/2}$. Similarly as before, estimating the regression coefficients for each regression window now gives us the values of $dD_{MP}/d\sqrt{P_{SW}}$ as a function of $\sqrt{P_{SW}}$.

[26] The left-hand side of Figure 3 shows the estimated derivatives of the function $D_{MP}(\sqrt{P_{SW}})$ and the corresponding error estimates. The function D_{MP} and its errors were estimated similarly as for the D_T and are depicted at the right-hand side of Figure 3. We find an almost perfect linear relationship between D_{MP} and $\sqrt{P_{SW}}$, in agreement with previous studies [e.g., *O'Brien and McPherron*, 2000]. The linear fit to the estimated D_{MP} values yields

$$D_{MP} = (11.84 \pm 0.04)\mathrm{nT}\sqrt{P_{SW}/\mathrm{nPa}}. \tag{21}$$

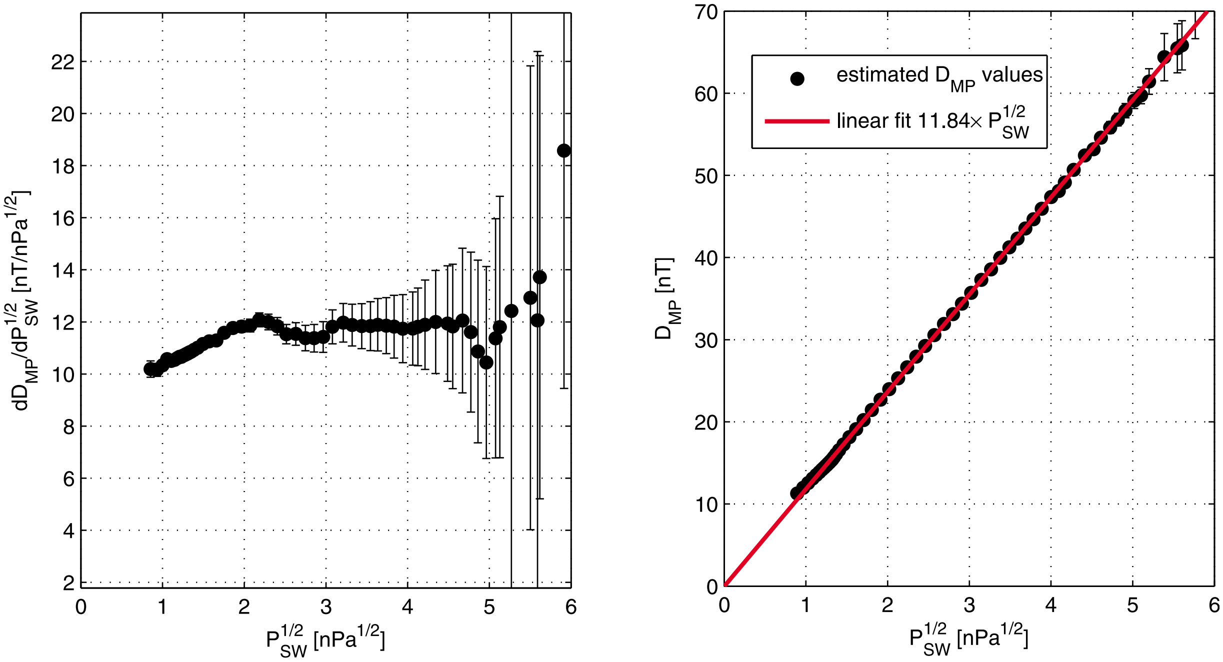

Figure 3. (left) Estimated derivative of $D_{MP}(\sqrt{P_{SW}})$ as a function of $\sqrt{P_{SW}}$. (right) Estimated $D_{MP}(\sqrt{P_{SW}})$ function (integral of the derivative on the left-hand side).

The constant of integration in determining D_{MP} was set so that D_{MP} is zero when $\sqrt{P_{SW}} = 0$ nPa. The obtained constant of proportionality is somewhat larger then the value 7.26 nT/nPa$^{1/2}$ given by *O'Brien and McPherron* [2000].

[27] Let us now rewrite equation (8) in the form

$$\frac{d(D_{CX} - D_T - D_{MP})}{dt} = Q + \frac{c}{\tau} - \frac{(D_{CX} - D_T - D_{MP})}{\tau}, \quad (22)$$

where the term $D_{CX} - D_T - D_{MP}$ is the contribution of the ring current to the *Dcx* index (except for the offset). We can now determine the ring current energy injection function Q and the ring current decay time τ by performing local linear regression to the above equation. In this regression the explaining variable is $D_{CX} - D_T - D_{MP}$ and the response variable the left-hand side of equation (22). Here both Q and τ are assumed to depend on the solar wind electric field and dynamic pressure. After experimenting with several combinations of E_{SW} and P_{SW} we found that the product $E_{SW}P_{SW}^{1/6}$ gives the best fit to the data. Local linear regression was performed by selecting 200 equally spaced values of $E_{SW}P_{SW}^{1/6}$ from the range [−20, 20] in units of mV/m nPa$^{1/6}$. About 97% of data points fall into this range (the range was not extended to cover all data points because of their sparsity at large values of $E_{SW}P_{SW}^{1/6}$). The length of the regression window was set to 2. From the regression coefficients β_1 of $D_{CX} - D_T - D_{MP}$ (i.e., the slope of the fit) we can solve the ring current decay time $\tau = -1/\beta_1$ and its error estimate $\Delta\tau = \Delta\beta_1/\beta_1^2$.

[28] Figure 4 shows the estimated ring current decay time τ as a function of $E_{SW}P_{SW}^{1/6}$. One can see that when the solar wind electric field is positive (southward IMF since $E_{SW} = -V_{SW}B_{IMF,Z}$) the decay time decreases rapidly from about 30 h to below 5 h with increasing $E_{SW}P_{SW}^{1/6}$, in agreement with earlier studies [see, e.g., *O'Brien and McPherron*, 2000]. For negative solar wind electric field (northward IMF) there is a large scatter in the decay time without any clear systematic trends. As suggested by *O'Brien and McPherron* [2000] the decrease of the decay time with increasing positive E_{SW} may be explained by the ring current shifting closer to the Earth (where the neutral atom density and consequently the probability of collision is higher) as E_{SW} increases. However, as noted by *O'Brien and McPherron* [2000], also other physical mechanisms may produce similar variation of τ with E_{SW}. We found that the functional form

$$\tau = A \exp\left(\frac{B}{C + E_{SW}P_{SW}^{1/6}}\right) \quad (23)$$

suggested by *O'Brien and McPherron* [2000] provides a good fit also here. Since τ behaves differently for positive and negative values of E_{SW}, we made separate fits for these two regions:

$$\tau = 2.031 \exp\left(\frac{19.199}{6.929 + E_{SW}P_{SW}^{1/6}}\right), \text{ for } E_{SW} \geq 0, \quad (24)$$

$$\tau = 22.7 \text{ h, for } E_{SW} < 0, \quad (25)$$

where the τ for negative E_{SW} is the median of τ values for $E_{SW} < 0$. We will next determine the offset level c by considering the constant term $\beta_0 = Q + c/\tau$ of the regression equation (22). The offset level can be estimated from those β_0 values for which Q can be assumed to be zero. Physically it is reasonable to expect that $Q \approx 0$ when the solar wind electric field E_{SW} is sufficiently negative. We selected from the estimated β_0 values those points where $E_{SW}P_{SW}^{1/6} < 0$ mV/m nPa$^{1/6}$ and computed the average value of $c = \beta_0\tau = -\beta_0/\beta_1$. The offset level

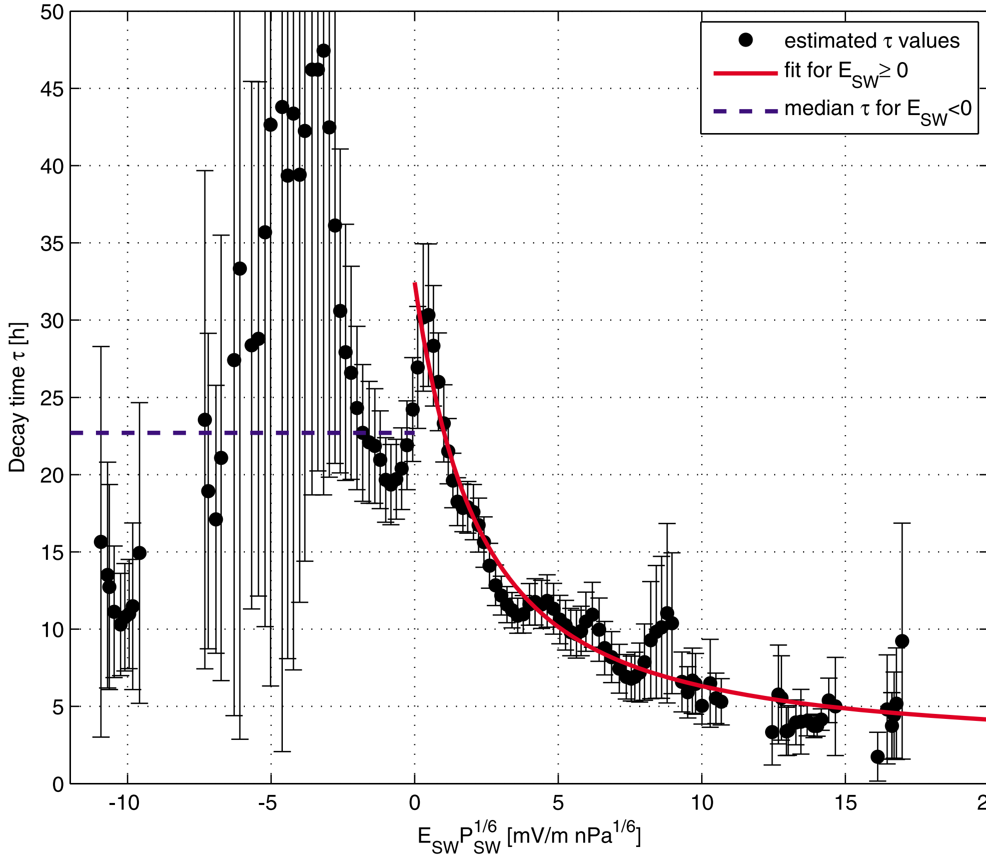

Figure 4. Estimated ring current decay time as a function of $E_{SW}P_{SW}^{1/6}$.

was roughly $c = -6$ nT. The quiet day average of $\sqrt{P_{SW}}$ during the internationally selected quiet days is 1.129 nPa$^{1/2}$ which yields a value of 13 nT for the quiet time level of the magnetopause currents. This indicates that the average quiet time level of the ring and tail currents is roughly −7 nT.

[29] As the last unknown parameter in the model we estimate the energy injection function Q from the constant term β_0 of the regression equation (22) by the expression $Q = \beta_0 - c/\tau$. Figure 5 shows the estimated Q and its error as a function of $E_{SW}P_{SW}^{1/6}$. We found that a good functional fit to the estimated values is provided by the expression

$$Q = -1.23\left[E_{SW}P_{SW}^{1/6}\right]^{1.283}, \text{ for } E_{SW}P_{SW}^{1/6} \geq 0$$
$$Q = 0, \text{ for } E_{SW}P_{SW}^{1/6} < 0. \tag{26}$$

It turns out that this expression tends to overestimate the injection rate into the ring current during a few extreme events (very large $E_{SW}P_{SW}^{1/6}$). To alleviate the situation we set a lower limit of −140 nT/h for Q corresponding to $E_{SW}P_{SW}^{1/6} \approx 40$. This lower limit was found to provide the best correlation between the modeled *Dcx* index and the original *Dcx* (see later).

[30] Finally, we note that determining the parameters of the model step by step in successive regressions should yield the same results as determining the simultaneously in one regression. We have checked that the correlation between the explaining variables is small and thus multicollinearity in the model should not cause a major bias in the parameter estimates. Also, proceeding with the regressions step by step is actually preferable in this case since determining the parameters simultaneously would require simultaneous controlling of MT, P_{SW} and E_{SW}. This would lead to a very low number of data points in most of the (MT, P_{SW}, E_{SW}) bins leading to statistically insignificant parameter estimates with large errors.

6. Reconstructing the *Dcx* Index Using the Model

[31] Let us now compute the model *Dcx* using the parameter functions determined above. We start by numerically solving the contribution of the ring current D_{RC} whose evolution is described by the differential equation

$$\frac{dD_{RC}}{dt} = Q(t) - \frac{D_{RC}}{\tau(t)}. \tag{27}$$

Both $Q(t)$ and $\tau(t)$ can be evaluated from the hourly solar wind/IMF data using equations (24)–(26). Equation (27) is integrated using the fourth-order Runge-Kutta algorithm, which gives the following recursive solution to D_{RC} at each time step:

$$D_{RC}(i+1) = D_{RC}(i) + \frac{1}{6}(k_1 + 2k_2 + 2k_3 + k_4), \tag{28}$$

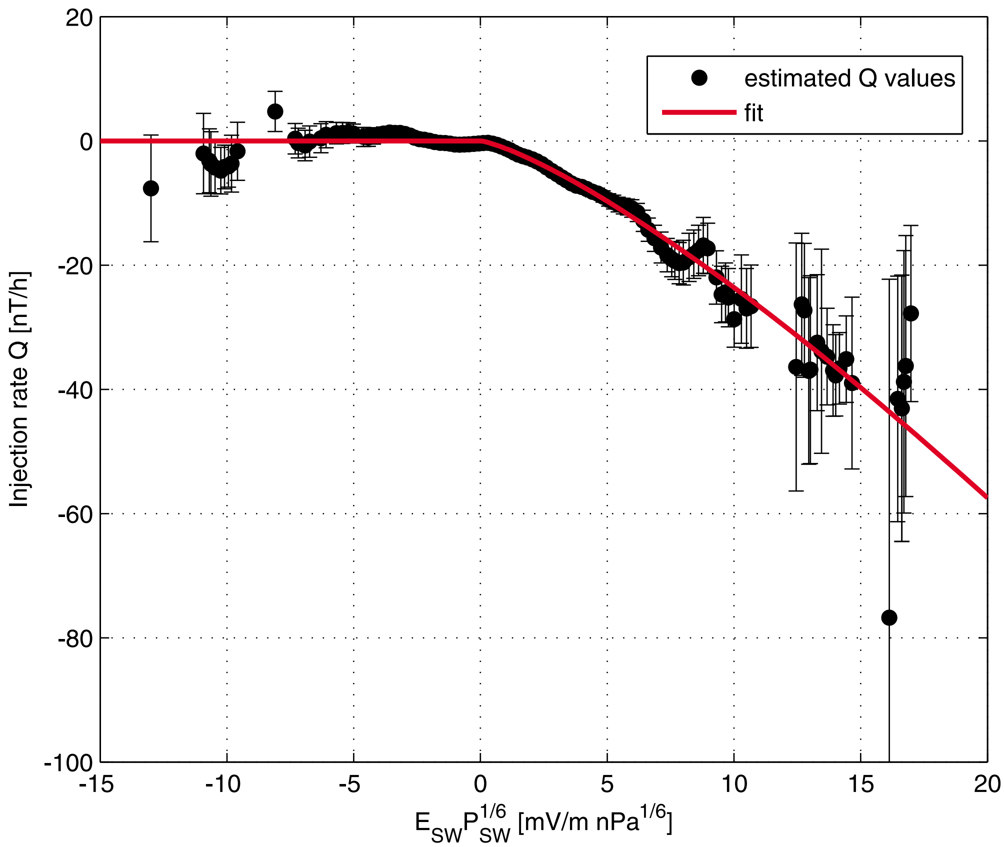

Figure 5. Estimated energy injection function Q as a function of $E_{SW}P_{SW}^{1/6}$.

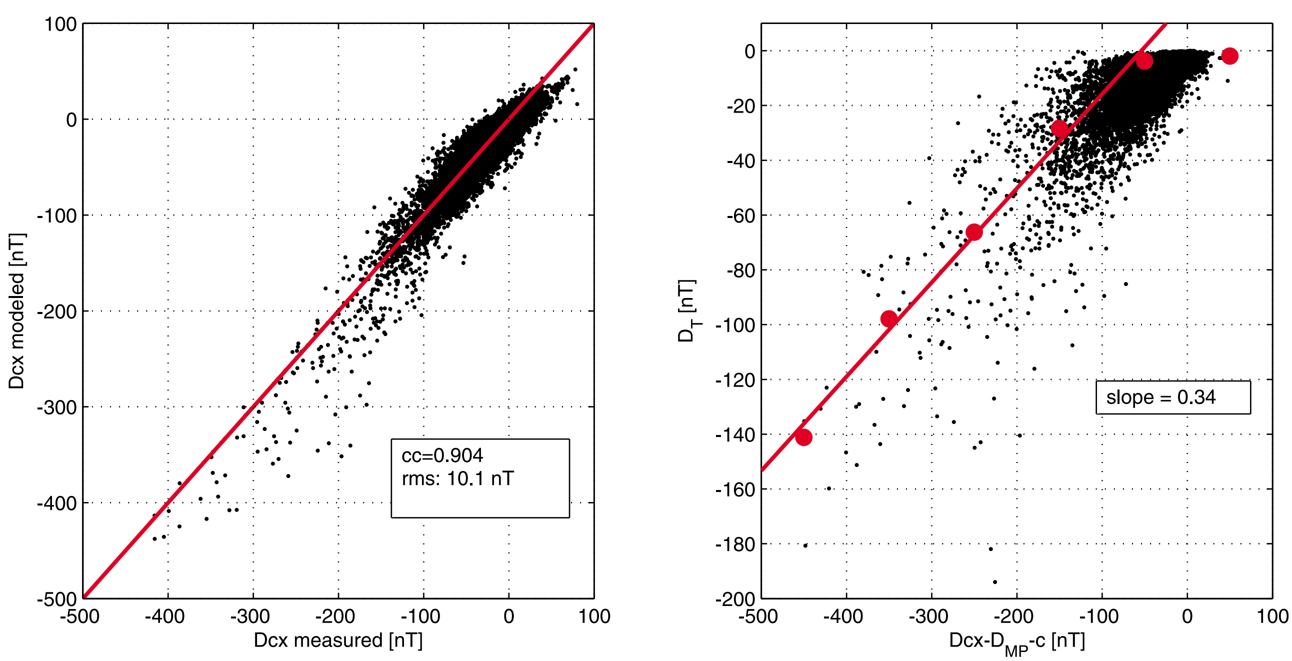

Figure 6. (left) The modeled *Dcx* versus measured *Dcx* with a line of unit slope for comparison. (right) Tail current contribution versus *Dcx* index corrected for solar wind pressure and offset. The red circles show the median D_T values within 100 nT wide bins of $D_{CX} - D_{MP} - c$. The line shows a linear fit to the median values.

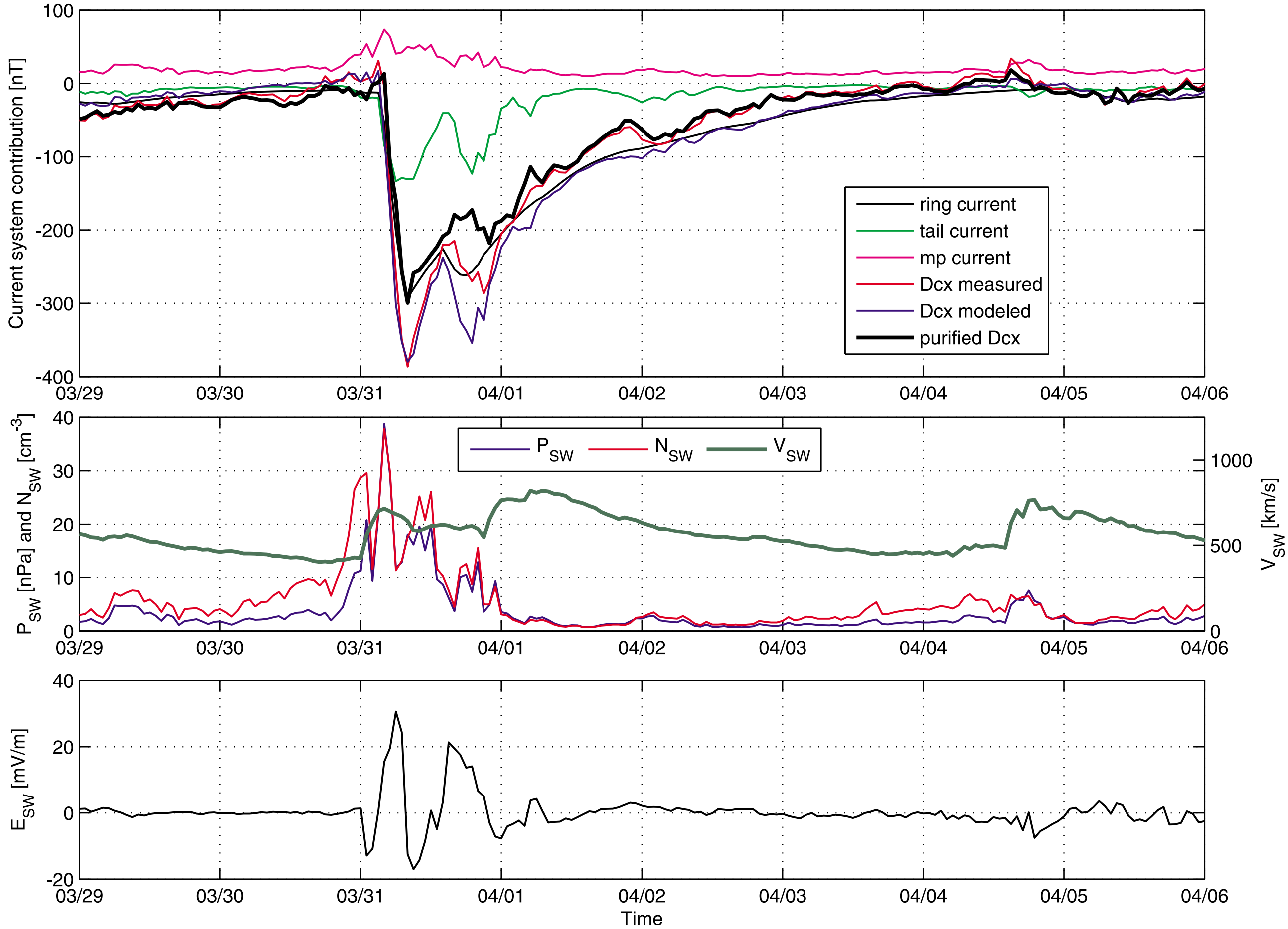

Figure 7. (top) The contributions of the different current systems to the *Dcx* during 29 March to 6 April 2001: ring current (thin black line), tail current (thin green line), magnetopause current (thin magenta line), measured *Dcx* (thin red line), modeled *Dcx* (thin blue line), and purified *Dcx* (thick black line). (middle) Solar wind pressure (P_{SW}, thin blue line), density (N_{SW}, thin red line), and velocity (V_{SW}, thick green line). Note that the pressure and the density have the same numerical scale. (bottom) Solar wind dawn-dusk electric field.

where the terms k_1, k_2, k_3, and k_4 are given by the expressions

$$k_1 = Q(i) - \frac{D_{RC}(i)}{\tau(i)}, \tag{29}$$

$$k_2 = Q(i+0.5) - \frac{D_{RC}(i) + 0.5k_1}{\tau(i+0.5)}, \tag{30}$$

$$k_3 = Q(i+0.5) - \frac{D_{RC}(i) + 0.5k_2}{\tau(i+0.5)}, \tag{31}$$

$$k_4 = Q(i+1) - \frac{D_{RC}(i) + k_3}{\tau(i+1)}. \tag{32}$$

In these expressions Q and τ at time steps $i + 0.5$ are calculated by linearly interpolating between the corresponding values at time steps i and $i + 1$. The initial value $D_{RC}(0)$ was estimated by the expression $D_{RC}(0) = D_{CX}(0) - D_T(0) - D_{MP}(0) - c$. The OMNI solar wind data contains many data gaps that can be several hours long during which Q and τ cannot be evaluated. During these times we estimate the value of the D_{RC} by a similar expression as the initial value; that is,

$$D^*_{CX}(i) = D_{CX}(i) - D_T(i) - D_{MP}(i) - c. \tag{33}$$

Here we have used linear interpolation to fill the data gaps in the D_T and D_{MP} time series. The modeled *Dcx* index is then calculated as the sum of different current system contributions and the offset, as expressed in equation (6) above. We also use equation (33) to estimate the ring current contribution for each time step, calling the corresponding index the purified *Dcx* index, *Dcx**. Such an estimate is inherently more accurate than the value obtained from the numerical solution of equation (27) since it uses fewer regression-based functional estimates. Note that when using equation (33) for the D_{RC} the different current system contributions and the offset term add up to the measured *Dcx* exactly.

[36] The left-hand side of Figure 6 shows the modeled *Dcx* values versus the measured *Dcx*. For comparison the plot includes a line with a unit slope. The correlation

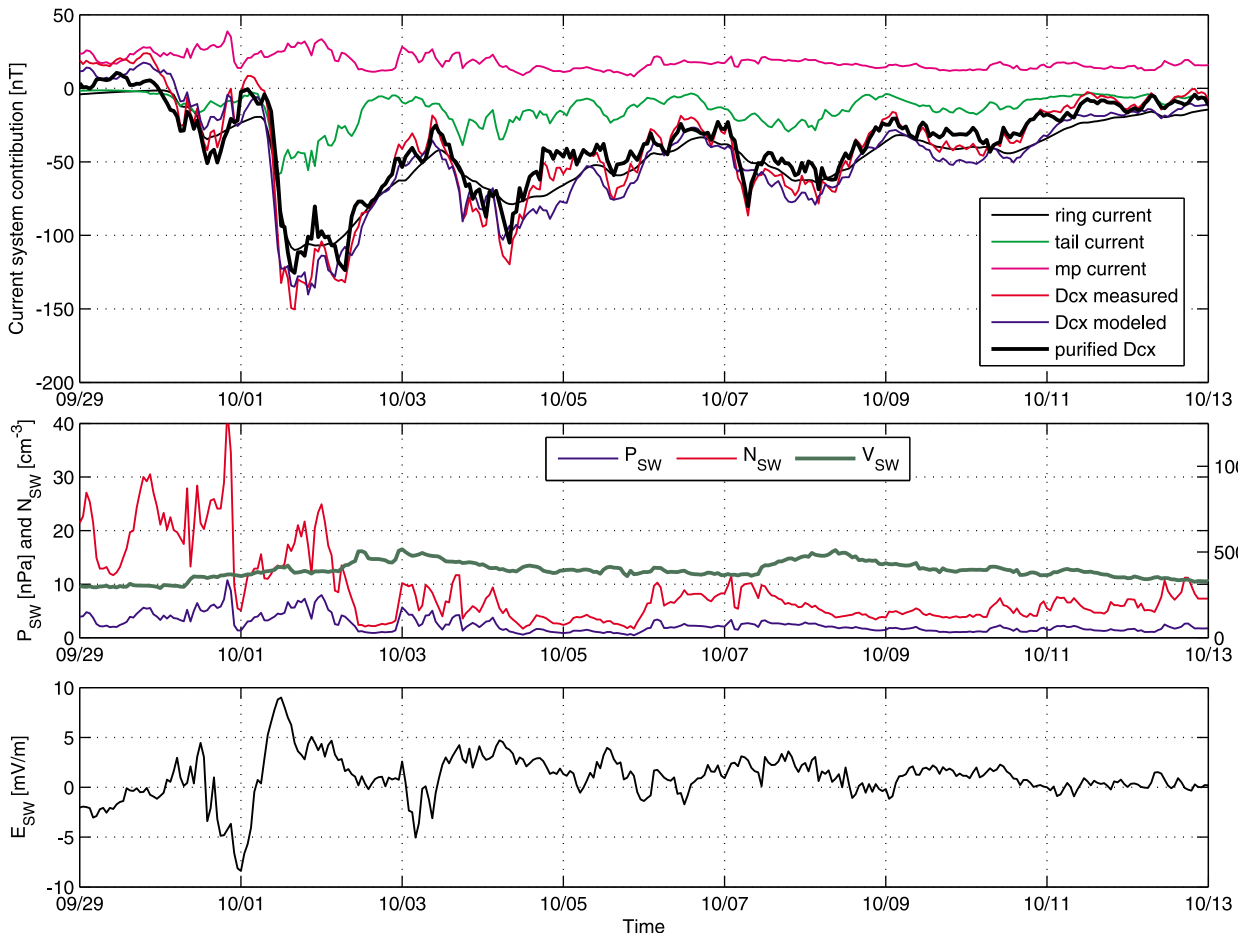

Figure 8. The contributions of the different current systems to the *Dcx* during 29 September to 13 October 2002. Panels and notations as in Figure 7.

coefficient between the two *Dcx* indices is 0.904, and the RMS deviation of the indices is 10.1 nT. When calculating the correlation coefficient and the RMS deviation we only included those points where there were no gaps in the solar wind data. One can see from Figure 6 that for 0 nT > *Dcx* > −150 nT there is no significant bias in the modeled *Dcx*. However, it seems that especially below −200 nT the model slightly overestimates the magnitude of the *Dcx*. For positive values of the *Dcx* the model tends to slightly underestimate the value of *Dcx*. Despite these deviations the overall correlation is good and indicates that more than 81% of the variation in *Dcx* could be explained by the model. Finally, it is important to note that the studied time period 1999–2007 contains both very quiet periods and extreme storms and that the model can roughly equally accurately produce the observed *Dcx* for all levels of activity. This shows that the dynamic ranges of the different current systems are well described by our model, unlike in many previous studies where the models fail during intense storms.

[37] The right-hand side of Figure 6 shows the contribution of the tail current D_T versus the measured *Dcx* index from which the contribution of solar wind pressure and the offset term have been subtracted. The red circles in the plot show the median D_T values calculated in 100 nT wide bins of $D_{CX} - D_{MP} - c$ and the line shows the linear fit to these median values. For nearly the whole range depicted the values of the tail current are roughly linearly related to the offset and solar wind pressure corrected *Dcx*. The slope of the regression line is 0.34 indicating that on average about 34% of the pressure corrected *Dcx* index comes from the tail current and roughly 66% comes from the ring current. The average fraction of the tail current contribution is essentially the same when comparing with raw *Dcx* values or values of D_T and *Dcx* during peak *Dcx* at storm times. This average fraction of the tail current contribution is slightly larger than estimates obtained earlier, about 25% by *Turner et al.* [2000] for the storm time peak values for storms with *Dst* > −100 nT. Estimating the average contribution of the tail current from the storm time peak values for storms with *Dcx* > −100 nT yields the same value of about 34%. However, taking all the points where *Dcx* > −100 nT yields about 20%. Thus, the results of *Turner et al.* [2000] are in the same range as our estimates. Furthermore, as can be seen from Figure 6, for major storms the D_T contribution is typically even somewhat larger than the average, about 30%–60% of the pressure and offset corrected *Dcx*. Finally, we note that even though there is a rough correlation between the pressure corrected *Dcx* and D_T the scatter is quite large indicating that

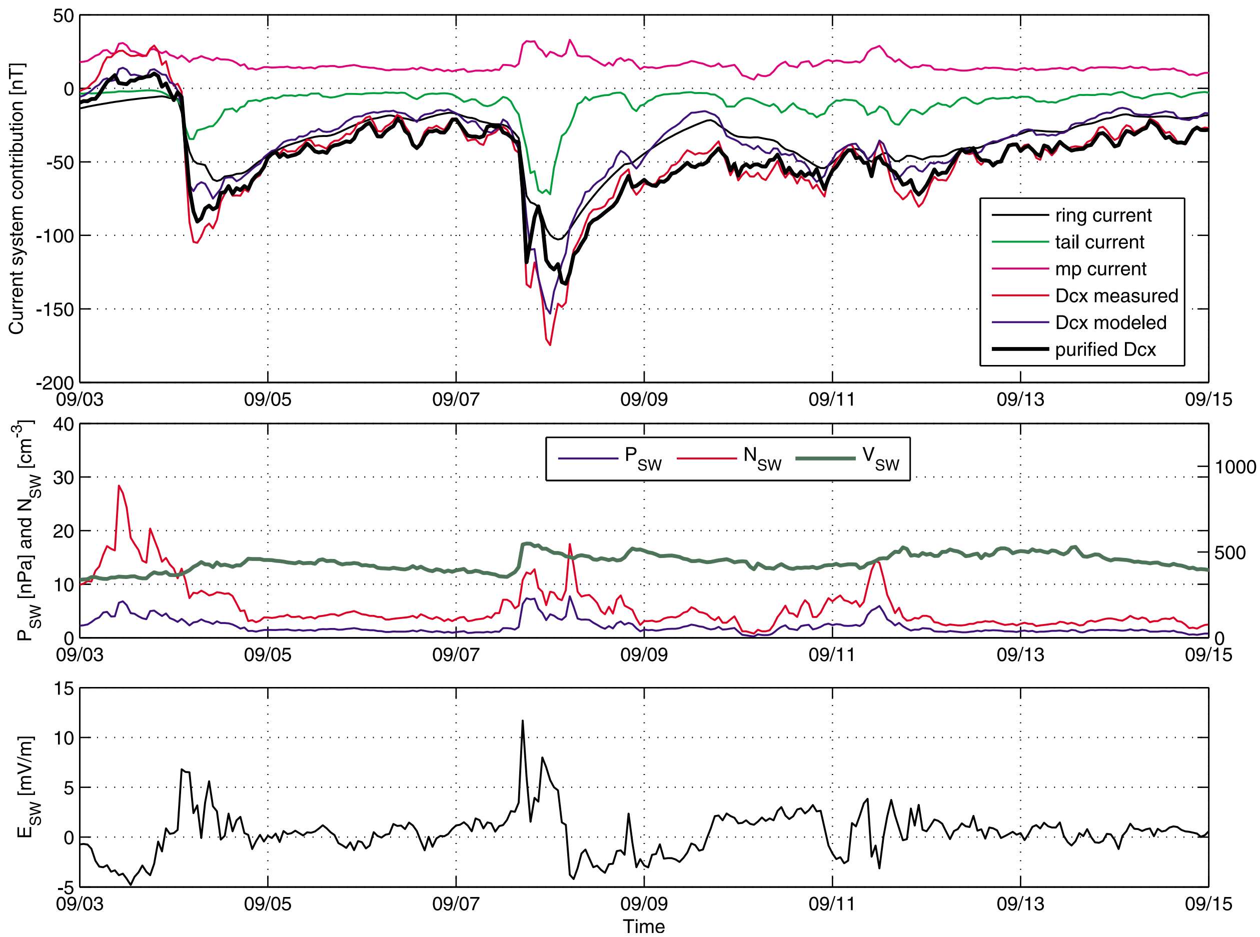

Figure 9. The contributions of the different current systems to the *Dcx* during 3–15 September 2002. Panels and notations as in Figure 7.

the dynamics of the ring and tail currents differ significantly from each other during individual storms.

7. Model Performance: A Few Case Studies

[38] Let us now study more closely the output of the model, i.e., the contributions of the different current systems to the *Dcx*, for a few selected events. The top panel in Figure 7 shows the different contributions to the *Dcx* for the widely studied storm of 31 March 2001 [e.g., *Asikainen et al.*, 2005], including the ring current contribution calculated from equation (27), the tail current, the magnetopause current as well as the measured, modeled and purified *Dcx* indices. For comparison, the middle panel of Figure 7 shows the solar wind pressure, density and velocity and the bottom panel shows the solar wind dawn-dusk electric field. One can see that during this very intense storm the model reproduces the observed *Dcx* rather well. The largest underestimation of the *Dcx* by about 80 nT occurs during the secondary enhancement of the *Dcx* during the latter half of 31 March. There is some systematic underestimation of the *Dcx* by the model also during the storm recovery phase. By far the largest contribution to the *Dcx* during this storm comes from the ring current. However, the tail current contribution is also very large (in absolute scale) reaching up to −130 nT. Note how the tail current contribution rapidly increases during the storm main phase but also starts to drop back rather fast, as the storm recovery begins. The tail current seems to react to IMF B_Z changes very sensitively.

[39] The purified *Dcx*, which is a more reliable estimate for the ring current, is systematically smaller in magnitude than the *Dcx* index with the largest difference being roughly 100 nT during the secondary enhancement of the *Dcx*. During the quiet times before and after the storm and the storm recovery phase the purified *Dcx* and the measured *Dcx* agree well. This indicates that at least during this storm the strongest contribution of the tail and the magnetopause currents to *Dcx* is concentrated mainly to the storm main phase. We note that the contributions of the ring, tail and magnetopause currents to the *Dst* during this storm were modeled by *Kalegaev and Makarenkov* [2006] using an analytic description of magnetospheric current systems that were parametrized by solar wind/IMF conditions. The time development of the tail current in their model shows the same fast variations as here and is overall quite similar to our model. Also the maximum contribution of the tail current to *Dst* was about −100 nT in their model, which is rather close to the maximum value found by our model.

[40] Figure 8 shows the contributions to the *Dcx* index and the solar wind parameters during a series of moderate storms between 29 September and 13 October 2002. Also during this time period the modeled *Dcx* follows the

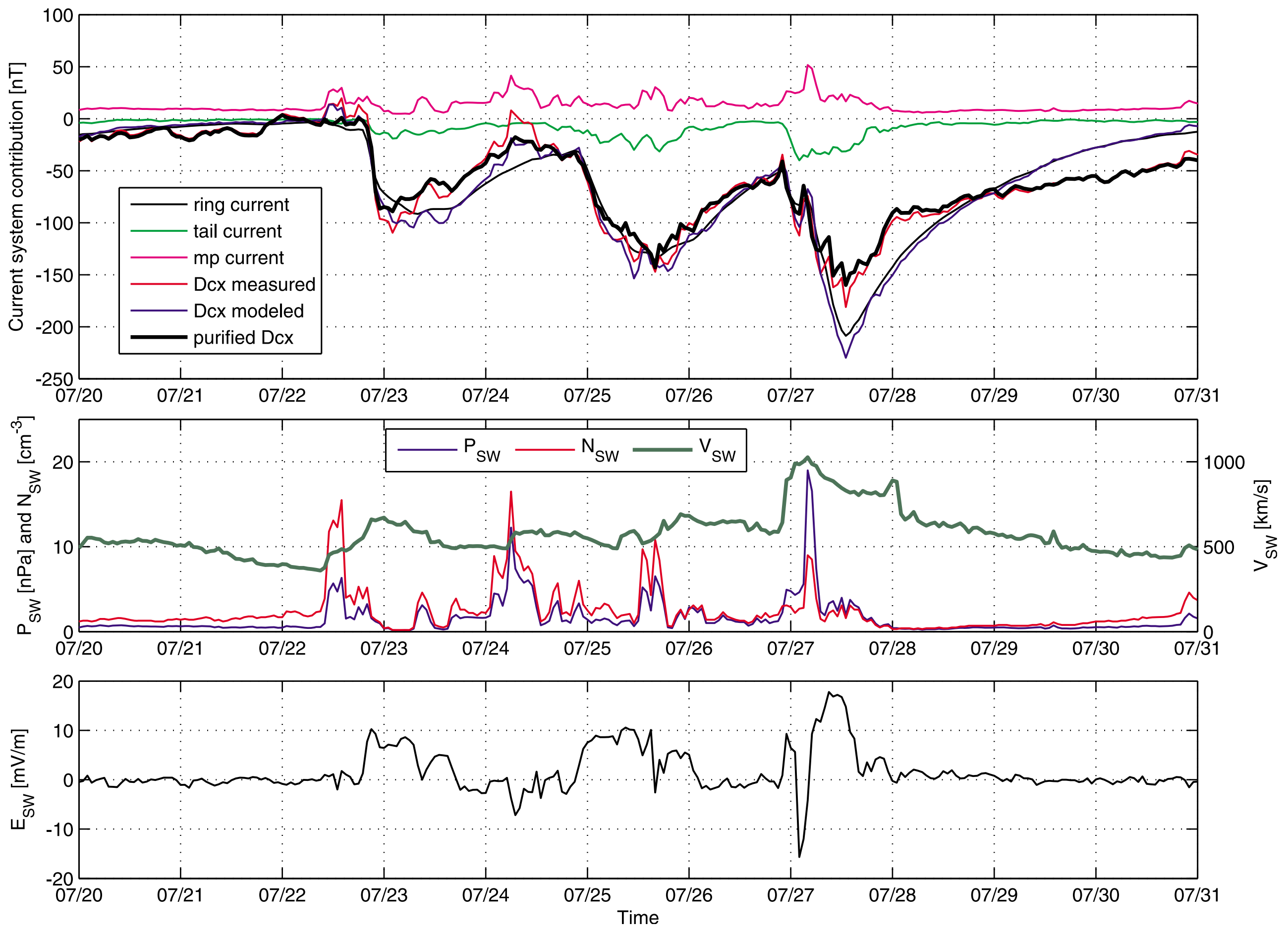

Figure 10. The contributions of the different current systems to the *Dcx* during 20–31 July 2004. Panels and notations as in Figure 7.

observed *Dcx* quite closely with the maximum difference being only about 30 nT during the most intense disturbances. Looking at the contributions of the different current systems it is obvious that also here the main contribution to *Dcx* comes from the ring current. The tail current contribution reaches up to about −50 nT during the main phase of the first storm and only to about −30 to −35 nT in the two subsequent main phases. The purified *Dcx* and the measured *Dcx* again agree very well during the quiet times and the recovery phases of these storms. The largest differences (about 35 nT) between the measured and purified *Dcx* indices again occur at the main phases of the storms when the tail current and magnetopause current contributions are largest.

[41] Figure 9 shows the components of the *Dcx* and the corresponding solar wind parameters during a couple of moderate storms during 3–15 September 2002. During this time period the model slightly overestimates the *Dcx* especially during the main phases of the two storms and the recovery phase of the second storm by about 20–40 nT. The tail current contribution is largest during the main phases of the storms reaching up to about −35 nT during the first storm and to about −70 nT during the second storm. The purified *Dcx* and the measured *Dcx* again closely agree during the quiet times and the recovery phases but differ significantly during the storm main phases especially during the second storm by over 50 nT. We note that this event was modeled by *Tsyganenko and Sitnov* [2005] and that their results are similar to ours. Especially the time development of the tail current during the storms is similar although the intensity of the tail current in our model during the first storm is about 30% smaller. However, during the second storm the tail current intensity and time development closely agree with the results of *Tsyganenko and Sitnov* [2005].

[42] Figure 10 shows the *Dcx* components and the solar wind parameters during the three-storm period of 22–30 July 2004. In this case the contribution of the tail current remains quite small throughout the event and is largely cancelled out by the magnetopause current. The modeled *Dcx* roughly follows the measured *Dcx* until the last enhancement in 27 July when the magnitude of the modeled *Dcx* seriously overestimates the measured *Dcx* index by about 65 nT. During the last recovery phase the model also fails by first overestimating and then underestimating the observed *Dcx* greatly. Interestingly, during the three successive storms the solar wind density decreases while the velocity increases especially during the last storm main phase to over 1000 km/s compared to the speed of about 600 km/s during the first two storms. This indicates that the model injection term Q, whose magnitude is now severely overestimated, probably depends on the solar wind velocity, density and IMF B_Z in a more complicated way than given by the functional rela-

tionship suggested above. A probable explanation is that the near-Earth space including the ionosphere is significantly preconditioned by the two previous storms in a way which our model, based on simultaneous values of the *Dcx*, MT and solar wind parameters, fails to capture. One effect of this preconditioning could be that the plasma sheet and/or ionospheric source population of the ring current ions is significantly depleted by the time the third main phase starts. It is likely that in this case the diminished solar wind density (which partly controls the plasma sheet density) limits the injection term in the last storm. Indeed, recently, *Weigel* [2010] showed that the solar wind density can significantly enhance the storm intensity. We note that we also tried to find an injection function and decay time that explicitly depend on solar wind density. However, all such functions produced a slightly smaller correlation coefficient and larger RMS error between the model and the measured *Dcx* than the injection function and τ presented above. Accordingly, solar wind pressure seems to be more important factor in determining the ring current injection and decay than the solar wind density, emphasizing the unique conditions during the three-storm event of Figure 10.

8. Summary and Conclusions

[43] In this paper we have developed a new semiempirical model to describe the contributions of the ring, tail and magnetopause currents to the *Dcx* index. We have used the location of the isotropic boundary obtained from the recently recalibrated fluxes of energetic particles, measured by the low-altitude NOAA/POES satellites, as a proxy for the tail current strength, obtaining an expression for the tail current contribution to the *Dcx* as a function of the IB latitude. Based on data from 1999 to 2007, the model gives the ring, tail and magnetopause current contributions not only during storms but for the whole time interval, performing roughly equally well during all activity levels albeit with a tendency to slightly underestimate the *Dcx* during extremely large storms. We have also verified that the magnetopause current contribution is linearly proportional to the square root of solar wind pressure but the coefficient of proportionality was found larger than in other recent estimates [e.g., *O'Brien and McPherron*, 2000]. We also find that the ring current decay time decreases with solar wind dawn-dusk electric field and dynamic pressure. We determined the average quiet time level of the ring and tail current contributions to *Dcx* to be roughly −7 nT while the average magnetopause contribution is about 13 nT. The tail current was found to cause, on an average, about 34% of the *Dcx* index, which is slightly larger than previous estimates for smaller intensity storms by, e.g., *Turner et al.* [2000]. During individual storms the tail current contribution can reach to over −160 nT (about 40%–60% of the pressure corrected *Dcx*). Despite the larger generality of the present model the intensity of different current systems and their time development during the individual storms agree well with the results of previous studies of some individual storms based on complicated dynamical models of the magnetosphere. Our work thus demonstrates that the different current system contributions to *Dcx* and their time development can be reliably estimated from the solar wind observations and the isotropic boundary measured by low-altitude satellites.

[44] **Acknowledgments.** We acknowledge support by the Academy of Finland to the postdoctoral project of T. Asikainen (134547) and to the HISSI research project 128189 and by the Thule Institute, University of Oulu. The research leading to these results has received funding from the European Commission's Seventh Framework Programme (FP7/2007-2013) under the grant agreement 218816 (SOTERIA project, www.soteria-space.eu).

[45] Philippa Browning thanks Vladimir Kalegaev and Frederick Rich for their assistance in evaluating this paper.

References

Akasofu, S.-I. (1981), Energy coupling between the solar wind and the magnetosphere, *Space Sci. Rev.*, *28*(2), 121–190.

Alexeev, I., E. Belenkaya, V. Kalegaev, Y. Feldstein, and A. Grafe (1996), Magnetic storms and magnetotail currents, *J. Geophys. Res.*, *101*(A4), 7737–7747.

Alexeev, I., et al. (2001), Dynamic model of the magnetosphere: Case study for January 9–12, 1997, *J. Geophys. Res.*, *106*(A11), 25,683–25,693.

Alexeev, I., E. Belenkaya, S. Bobrovnikov, and V. Kalegaev (2003), Modeling the electromagnetic field in the interplanetary space and in the Earth's magnetosphere, *Space Sci. Rev.*, *107*(1/2), 7–26.

Asikainen, T., and K. Mursula (2010), Recalibration of NOAA/MEPED energetic proton measurements, *J. Atmos. Sol. Terr. Phys.*, doi:10.1016/j.jastp.2009.12.011, in press.

Asikainen, T., R. Kerttula, K. Mursula, R. Friedel, D. Baker, F. Søraas, J. Fennell, and J. Blake (2005), Global view of energetic particles during a major magnetic storm, in *The Inner Magnetosphere: Physics and Modeling*, *Geophys. Monogr. Ser.*, vol. 155, edited by T. Pulkkinen, N. Tsyganenko, and R. Friedel, pp. 97–104, AGU, Washington, D. C.

Ballatore, P., and W. Gonzalez (2003), On the estimates of the ring current injection and decay, *Earth Planets Space*, *55*, 427–435.

Burton, R., R. McPherron, and C. Russell (1975), An empirical relationship between interplanetary conditions and Dst, *J. Geophys. Res.*, *80*(31), 4204–4214.

Chen, J. (1992), Nonlinear dynamics of charged particles in the magnetotail, *J. Geophys. Res.*, *97*(A10), 15,011–15,050.

Daglis, I. A. (1997), The role of magnetosphere-ionosphere coupling in magnetic storm dynamics, in *Magnetic Storms*, *Geophys. Monogr. Ser.*, vol. 98, edited by B. Tsurutani et al., pp. 107–116, AGU, Washington, D. C.

Daglis, I., R. Thorne, W. Baumjohann, and S. Orsini (1999), The terrestrial ring current: Origin, formation, and decay, *Rev. Geophys.*, *37*, 407–438.

Dessler, A., and E. Parker (1959), Hydromagnetic theory of geomagnetic storms, *J. Geophys. Res.*, *64*(12), 2239–2252.

Evans, D. S., and M. S. Greer (2000), Polar orbiting environmental satellite space environment monitor: 2. Instrument descriptions and archive data documentation, *Tech. Memo. OAR SEC-93*, NOAA, Boulder, Colo.

Feldstein, Y., A. Grafe, V. Pisarskij, V. Yu, A. Prigancová, and P. Surnaruk (1990), Magnetic field of the magnetospheric ring current and its dynamics during magnetic storms, *J. Atmos. Terr. Phys.*, *52*, 1185–1191.

Ganushkina, N., T. Pulkkinen, M. Kubyshkina, H. Singer, and C. Russell (2004), Long-term evolution of magnetospheric current systems during storms, *Ann. Geophys.*, *22*, 1317–1334.

Gonzalez, W., B. Tsurutani, A. Gonzalez, E. Smith, F. Tang, and S.-I. Akasofu (1989), Solar wind-magnetosphere coupling during intense magnetic storms (1978–1979), *J. Geophys. Res.*, *94*(A7), 8835–8851.

Gonzalez, W., J. Joselyn, Y. Kamide, H. Kroehl, G. Rostoker, B. Tsurutani, and V. Vasyliunas (1994), What is a geomagnetic storm?, *J. Geophys. Res.*, *99*(A4), 5771–5792.

Hill, V. J., D. S. Evans, and H. H. Sauer (1985), TIROS-N/NOAA satellites Space Environment Monitor archive tape documentation, *Tech. Memo. ERL SEL-71*, NOAA, Boulder, Colo.

Huber, P. (1964), Robust estimation of a location parameter, *Ann. Math. Stat.*, *35*, 73–101.

Kalegaev, V., and E. Makarenkov (2006), Dynamics of magnetospheric current systems during magnetic storms of different intensity, *Geomagn. Aeron.*, *46*(5), 570–579.

Kalegaev, V., N. Ganushkina, T. Pulkkinen, M. Kubyshkina, H. Singer, and C. Russell (2005), Relation between the ring current and the tail current during magnetic storms, *Ann. Geophys.*, *23*, 523–533.

Karinen, A., and K. Mursula (2005), A new reconstruction of the Dst index for 1932–2002, *Ann. Geophys.*, *23*, 475–485.

Karinen, A., K. Mursula, J. Takalo, and T. Ulich (2002), An erroneous Dst index in 1971, in *SOLSPA 2001: Proceedings of the Second Solar Cycle and Space Weather Euroconference: 24–29 September 2001, Vico Equense, Italy, ESA SP*, vol. 477, pp. 443–446, Eur. Space Agency, Noordwijk, Netherlands.

MacMahon, R. M., and C. Llop-Romero (2008), Ring current decay time model during geomagnetic storms: A simple analytical approach, *Ann. Geophys.*, *26*, 2543–2550.

Mursula, K., and A. Karinen (2005), Explaining and correcting the excessive semiannual variation in the Dst index, *Geophys. Res. Lett.*, *32*, L14107, doi:10.1029/2005GL023132.

Mursula, K., L. Holappa, and A. Karinen (2008), Correct normalization of the Dst index, *Astrophys. Space Sci. Trans.*, *4*, 41–45.

Mursula, K., L. Holappa, and A. Karinen (2010), Uneven weighting of stations in the Dst index, *J. Atmos. Sol. Terr. Phys.*, doi:10.1016/j.jastp.2010.04.007, in press.

O'Brien, T., and R. McPherron (2000), An empirical phase space analysis of ring current dynamics: Solar wind control of injection and decay, *J. Geophys. Res.*, *105*(A4), 7707–7719.

O'Brien, T., and R. McPherron (2002), Seasonal and diurnal variation of Dst dynamics, *J. Geophys. Res.*, *107*(A11), 1341, doi:10.1029/2002JA009435.

Raben, V. J., D. S. Evans, H. H. Sauer, S. R. Sahm, and M. Huynh (1995), TIROS/NOAA satellite Space Environment Monitor data archive documentation: 1995 update, *Tech. Memo. ERL SEL-86*, NOAA, Boulder, Colo.

Sckopke, N. (1966), A general relation between the energy of trapped particles and the disturbance field near the Earth, *J. Geophys. Res.*, *71*(13), 3125–3130.

Seale, R. A., and R. H. Bushnell (1987), The TIROS-N/NOAA A-J Space Environment Monitor subsystem, *Tech. Memo. ERL SEL-75*, NOAA, Boulder, Colo.

Sergeev, V., and B. Gvozdevsky (1995), MT-index: A possible new index to characterize the magnetic configuration of magnetotail, *Ann. Geophys.*, *13*, 1093–1103.

Sergeev, V., and N. Tsyganenko (1982), Energetic particle losses and trapping boundaries as deduced from calculations with a realistic magnetic field model, *Planet. Space Sci.*, *30*, 999–1007.

Sergeev, V., M. Malkov, and K. Mursula (1993), Testing the isotropic boundary algorithm method to evaluate the magnetic field configuration in the tail, *J. Geophys. Res.*, *98*(A5), 7609–7620.

Siscoe, G., V. Formisano, and A. Lazarus (1968), Relation between geomagnetic sudden impulses and solar wind pressure changes: An experimental investigation, *J. Geophys. Res.*, *73*(15), 4869–4874.

Søraas, F., K. Aarsnes, and K. Oksavik (2002), Ring current intensity estimated from low-altitude proton observations, *J. Geophys. Res.*, *107*(A7), 1149, doi:10.1029/2001JA000123.

Sugiura, M., and T. Kamei (1991), *Equatorial Dst Index* 1957–1986, ISGI, Saint-Maur-des-Fossés, France.

Temerin, M., and X. Li (2002), A new model for the prediction of Dst on the basis of the solar wind, *J. Geophys. Res.*, *107*(A12), 1472, doi:10.1029/2001JA007532.

Tsyganenko, N., and M. Sitnov (2005), Modeling the dynamics of the inner magnetosphere during strong geomagnetic storms, *J. Geophys. Res.*, *110*, A03208, doi:10.1029/2004JA010798.

Turner, N., D. Baker, T. Pulkkinen, and R. McPherron (2000), Evaluation of the tail current contribution to Dst, *J. Geophys. Res.*, *105*(A3), 5431–5439.

Wang, C., J. Chao, and C.-H. Lin (2003), Influence of the solar wind dynamic pressure on the decay and injection of the ring current, *J. Geophys. Res.*, *108*(A9), 1341, doi:10.1029/2003JA009851.

Weigel, R. S. (2010), Solar wind density influence on geomagnetic storm intensity, *J. Geophys. Res.*, *115*, A09201, doi:10.1029/2009JA015062.

T. Asikainen, V. Maliniemi, and K. Mursula, Department of Physics, PO Box 3000, University of Oulu, Oulu FI-90014, Finland. (timo.asikainen@oulu.fi)